Sensor Installation and Retrieval Operations using an Unmanned Aerial Manipulator

S. Hamaza[1], I. Georgilas[2], M. Fernandez[3], P. Sanchez[3], T. Richardson[1], G. Heredia[3], A. Ollero[3]

Abstract—A wide range of applications for which Unmanned Aerial Vehicles (UAVs) are ideally suited rely on the development of manipulators capable of exchanging forces with the environment. One such application is the installation and retrieval of intelligent sensors for monitoring wide-spread areas and locations that are difficult to access by any other means. Within this paper we report on both indoor and outdoor flights tests of a novel force controlled lightweight compliant manipulator which allows a UAV to carry out this type of task. Installation and retrieval are both demonstrated with different scenarios, indoors and outdoors. Key results include interaction forces up to 22 N exerted by a small-sized multirotor; placement and retrieval operations carried out on flat as well as cylindrical surfaces; and an analysis of the overall system. The results of multiple flight experiments clearly demonstrate the potential of this approach for the deployment of sensors and other force-related tasks.

Index Terms—Aerial Systems: Applications; Aerial Systems: Mechanics and Control; Mechanism Design.

I. INTRODUCTION

A fast growing interest in the field of UAVs in the past two decades has brought the research community to explore further ways in which these agile compact platforms can be exploited. Visual sensing for UAVs has propelled a variety of tasks such as environmental surveying, search and rescue, traffic monitoring, surveillance, and broadcasting. These successful applications are mostly limited to passive observation, however huge potential lies in tasks that require physical interaction with the environment [1].

UAVs can be equipped with mechanical devices to enable airborne manipulation tasks. The two most adopted solutions are either to mount a gripper or multi-fingered hand directly at the aerial vehicle's frame [2]–[4], which provide limited object manipulation capabilities and are most suited for grasping operations, or to equip the UAV with one or more robotic arms, e.g., an Unmanned Aerial Manipulator (UAM).

UAMs are capable of exchanging forces with the environment and carrying out inspection and maintenance tasks. Some example scenarios in which UAMs could be deployed are the potential repair of cracks on wind turbine blades,

Fig. 1: A small-sized quadcopter equipped with the bespoke lightweight manipulator performs installation of a sensor on a tree.

cleaning of clogged-up thermocouples on top of high industrial chimneys, contact-based inspection of bridges and dams, or the installation and retrieval of intelligent sensors in wide-spread areas or infrastructure. These applications have been the case study of several projects over the years, e.g. [5]–[7].

So far research in the field of aerial manipulation has progressed from load transportation by a single [2] or multiple UAVs [8], to non-destructive testing (NDT) [9], valve turning [10], assembly tasks [3] and bridge inspection [11]. Several manipulator's designs have been proposed, ranging from the use of commercially available robotic arms [12], to more customised lightweight solutions [13]–[15] or parallel structures such as delta robots [9].

The application of force to the environment is addressed in the following studies: in [16], [17] the ability to exert contact forces up to 5 N in quasi-static condition, i.e. interaction carried out with the UAV in hover state, is demonstrated. In [18] the ability of the UAM to operate in highly dynamical conditions is presented, with the case study of collision absorbance thanks to a passively-compliant element. In [19] a compact UAM comprising adaptive compliance can tune the force exerted on a wall by adjusting the manipulator's compliance parameters. In [20] successful application of substantial force is achieved through the use of a tilt-rotor UAV. In [21] substantial forces of up to 16 N are exerted by a quadrotor pitching at high angles, converting the aircraft thrust into a force normal to the contact surface.

The key contribution of this work lies in the novel approach to force exertion by a UAM using a compliant active manipulator for the autonomous placement and recovery of sensors within a realistic environment. Differently from the current state-of-the-art, the force output of the end-effector results from the active manipulator combined with the UAV's pitching motion and on-board sensing, and allows to have a compliant

approach with the target surface and a slow force build-up. The manipulator's novel configuration integrates the vehicle states, resulting in closed loop control within the manipulator itself to generate the desired force response. Such force-driven operations are repeatedly tested for the placement and retrieval of sensors in the environment, with forces up to 22 N generated by the UAM.

The outline of this paper presents the design considerations and manufacturing of the manipulator, followed by the modeling of the aerial system. The next section illustrates the overall system architecture and control, followed by indoor and outdoor experiments sections. The results show the contact and retrieval phases of the flight, the corresponding vehicle response and the forces generated throughout. The video attachment illustrates the repeatability and robustness of this approach in different conditions.

II. MANIPULATION SYSTEM

A. Design Considerations

In general, the approach found in the literature when it comes to designing a UAM is to use serial manipulators with n-joints providing n-DoFs. However, despite the dexterity that a higher-DoF manipulator allows in terms of tasks that can be accomplished, the major drawback for the aircraft is the added weight, impacting on manoeuvrability and battery life. Hence, it is essential to limit the weight where possible and avoid redundancy whilst still devising the right tool for the job. For contact-based tasks that require the exertion of a force normal to a surface, e.g. NDT or installation of sensors, a simple probe oriented towards the contact surface provides a minimal, weight-efficient solution to the problem.

As demonstrated in [22], it is important to minimise the inertias of the UAM by keeping to a compact design and by moving the contact point as close as possible to the aircraft CoG. Moreover, by reducing the misalignment between the contact point and the aircraft CoG, the momentum induced by the interaction is also reduced, bringing a benefit to the overall stability. To achieve this, the end-effector is oriented towards the CoG by means of an inclined support, featuring design parameter ϕ illustrated in Fig. 3.

Lastly, it is desirable to avoid moving masses in flight, and to group the heavier components of the manipulator as close as possible to the UAV's CoG in order to maximise the vehicle dynamic response.

B. Manipulator Design

We propose a single-DoF manipulator comprising a prismatic joint that acts as a mechanical impedance tool on the environment: as the link slides within the joint, the end-effector protrudes out and generates a force that varies in direction and module depending on the task requirements.

The slider is embodied by a rack and pinion mechanism, driven by a high-performance motor controller. Besides being lightweight, another advantage of this compact design is that it minimises the effect on the vehicle stability when compared to retractable arms, as no moving masses are present except for the sliding rack itself ($\approx$ 90g).

The rack and pinion components are manufactured in aluminium to ensure a more accurate transmission and reduce the overall mass. Two ball bearings hold the pinion in place and release the motor from any radial tension that might be generated during interaction. Similarly, two linear bearings ensure adherence of the rack's teeth in the linear coupling. In Fig. 2 the transmission mechanism is illustrated.

A brushless DC motor drives the pinion directly, i.e. no gear reduction is present, and provides a nominal torque T_{nom} of 83.4 mNm and stall torque T_{stall} of 780 mNm. The main reason for selecting this particular motor is that it allows to counteract high forces that might generate during the initial impact of the rack against the target surface. The torque module T needed by the motor to counteract an interaction force F_{int} on the rack is:

$$T = F_{int} \; r_p \leq T_{stall} \qquad (1)$$

where r_p is the radius of the pinion pitch circle, in our case r_p = 2.5 mm. Therefore the nominal force that the motor can generate or receive on the pinion is $F_{nom} = T_{nom}/r_p = 33.3$ N, and the maximum force over a short period (e.g. 3 s) would be $F_{max} = T_{stall}/r_p = 312$ N. This represents a safe upper bound for the motor to operate in case of impacts.

Lastly, the manipulator is equipped with 2 sensors: a rangefinder mounted at the front of the aircraft to measure the distance between the vehicle and obstacles ahead; and an inductive encoder on the manipulator which measures the relative position of the end-effector.

C. End-Effectors

Two different end-effectors are used for sensor installation and retrieval in this paper. For the placement task, magnetic force is used to hold the sensor in place during flight and installation. The tip of the rack is equipped with a flat surface that resembles a lid. Onto this surface an array of magnets is placed in such a way to avoid repulsion forces between them. The same configuration is replicated on the outside of the sensor case, by mirroring the magnets. The adhesion force produced by the magnets F_{grip} must be enough to carry the sensor itself and overcome the forces generated by aerodynamic disturbances in flight, especially during take-off and in vicinity of the wall, but must be low enough to allow the adhesive pad to dominate during sensor placement:
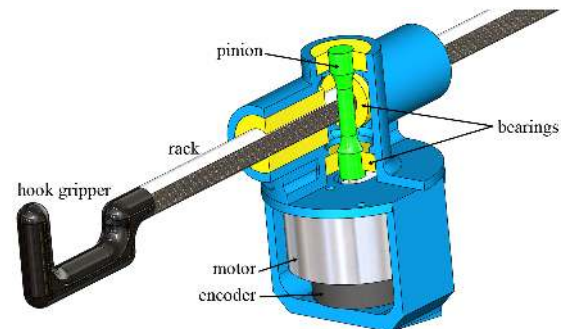
$$F_{grip} \geq m_s g + F_{dist} \qquad (2)$$

Fig. 2: Cross section CAD drawing of the pinion-rack mechanism.

where m_s is the mass of the sensor ($\approx$ 40g), g is the gravitational acceleration and F_{dist} is the force due to disturbances in flight, e.g. turbulence generated by the surrounding propellers during take-off, or the wall-effect. The computation of F_{grip} can be quite complex, especially because the force due to disturbances is unknown and varies for each flight. However, a reliable adhesion between the end-effector and the sensor was achieved with 2.5 cm^2 magnetic surface, experiencing a negligible failure rate, i.e. below 2%.

The end-effector devised for the retrieval task is a long open hook, attached to the rack by means of a screw (see Fig. 2). This design is selected as it facilitates the grasp and for its simplicity. On the sensor a metal loop is provided through which the hook can engage with the object and stabilise the contact during the pull phase.

III. MODELING

In this section the kinematics and dynamics of the system are analysed and discussed, the solution of which will be used in the *Control* section (section IV).

A. Kinematics

Let us consider a UAV with 1-DoF manipulator as depicted in Fig. 3. We consider three coordinate frames to describe the kinematics of this rigid body in space: the world frame $\mathcal{W}$, the body-fixed frame $\mathcal{A}$ centred in the aircraft CoG and the end-effector frame $\mathcal{E}$ centred in the contact point. Let us define three pose vectors: $\pi_{\mathcal{A}}^{\mathcal{W}}$ describes the pose of the aircraft with respect to the world frame, vectors $\pi_{\mathcal{E}}^{\mathcal{W}}$ and $\pi_{\mathcal{E}}^{\mathcal{A}}$ describe the pose of the end-effector with respect to the world and aircraft frame respectively. All vectors π comprise of translational and rotational terms about the *x-y-z* axes.

Now, due to the nature of the UAV of being an underactuated platform, the dynamics governing the vehicle cannot be decoupled from the dynamics of the manipulator, as disturbances in the *roll-pitch-yaw* angles affect the position of the end-effector. Hence the kinematic chain $\chi = [\zeta_x \ \zeta_y \ \zeta_z \ \phi \ \theta \ \psi \ \mathbf{q}]^T$ describes the two systems as a single, where χ represents a $(6 + 1)$ dimension vector consisting of the aircraft linear and rotational terms, and the manipulator's generalised coordinates vector, $\mathbf{q}$. The position of the end-effector with respect to the world frame $\pi_{\mathcal{E}}^{\mathcal{W}}$ combines the (4

Fig. 3: Sketch of the aerial manipulator with coordinate frames and relevant parameters.

$\times$ 4) homogeneous transformation matrices $\mathbf{T}_{\mathcal{A}}^{\mathcal{W}}$ and $\mathbf{T}_{\mathcal{E}}^{\mathcal{A}}$ of the aircraft and the manipulator respectively, as follows:

$$\pi_{\mathcal{E}}^{\mathcal{W}} = \pi_{\mathcal{A}}^{\mathcal{W}} + \mathbf{R}_{\mathcal{E}}^{\mathcal{A}} \pi_{\mathcal{E}}^{\mathcal{A}} = \mathbf{T}_{\mathcal{E}}^{\mathcal{W}}(\chi) =$$
$$= \mathbf{T}_{\mathcal{A}}^{\mathcal{W}}(\zeta_x \ \zeta_y \ \zeta_z \ \phi \ \theta \ \psi) \ \mathbf{T}_{\mathcal{E}}^{\mathcal{A}}(\mathbf{q}) \quad (3)$$

where $\mathbf{R}_{\mathcal{E}}^{\mathcal{A}}$ is the rotation matrix from frame $\mathcal{A}$ to $\mathcal{E}$.

Figure 3 shows each frame's orientation used to solve the forward kinematics problem. Without loss of generality, it is assumed that the aircraft frame is located at the base of the prismatic joint, since the vehicle CoG and the manipulator's CoG almost coincide. Frame $\mathcal{E}$ has the *z-axis* $z_{\mathcal{E}}$ in blue aligned with the end-effector; frame $\mathcal{A}$ is rotated clockwise about $x_{\mathcal{E}}$ of an angle of $90° + \phi$, where ϕ takes into account the small inclination of the prismatic joint on the platform. The distance between the origins of frames $\mathcal{A}$ and $\mathcal{E}$ varies with the length of the slider, namely variable ℓ. The Denavit-Hartenberg parameters are: $a_0 = 0, \alpha_0 = 90° + \phi, \ d_1 = \ell$ and $\theta_1 = 0$. Hence:

$$\mathbf{T}_{\mathcal{E}}^{\mathcal{A}}(\mathbf{q}) = \begin{bmatrix} 1 & 0 & 0 & 0 \\ 0 & cos(\alpha_0) & -sin(\alpha_0) & -\ell sin(\alpha_0) \\ 0 & sin(\alpha_0) & cos(\alpha_0) & \ell cos(\alpha_0) \\ 0 & 0 & 0 & 1 \end{bmatrix} \quad (4)$$

Knowing the extension of the rack ℓ by means of an on-board encoder, and the angle α_0 as part of the manipulator's design, the forward kinematics problems is solved.

B. Dynamics

In a quadcopter, the general thrust produced by each propeller i, $\mathbf{T}(u)^i$ is directed along the *z-axis* in the body-fixed frame $\mathcal{A}$. Similarly the torque $\boldsymbol{\tau}(u)^i$ generated by each rotor is about the same axis, $z_{\mathcal{A}}$. The summation of all $\mathbf{T}(u)^i$ generates the total thrust of the aircraft, $\mathbf{F}_a(u)$, measured about frame $\mathcal{W}$ are:

$$\mathbf{F}_a(u) = \sum_{i=1}^{4} \mathbf{T}(u)^i \quad (5)$$

$$\boldsymbol{\tau}_a(u) = \sum_{i=1}^{4} \boldsymbol{\tau}(u)^i + \Delta\mathbf{r}_i \times \mathbf{T}(u)^i \quad (6)$$

where vector $\Delta\mathbf{r}_i$ represents the distance of each propeller from the aircraft CoG in $\mathcal{A}$. This force needs to counterbalance the weight of the platform $\mathbf{F}_g = -mg$, as well as other non-linear aerodynamic effects, e.g. gusts, turbulence due to the wall-effect, and the presence of the manipulator. The equations of motion of the manipulation system can be derived using the Newton-Euler approach:

$$\begin{bmatrix} \mathbf{F}_m(\mathbf{q}, \dot{\mathbf{q}}, \ddot{\mathbf{q}}) \\ \boldsymbol{\tau}_m(\mathbf{q}, \dot{\mathbf{q}}, \ddot{\mathbf{q}}) \end{bmatrix} = \mathbf{M}(\mathbf{q})\ddot{\mathbf{q}} + \mathbf{C}(\mathbf{q}, \dot{\mathbf{q}})\dot{\mathbf{q}} + \mathbf{G}(\mathbf{q}) \quad (7)$$

with $\mathbf{M}$ being the mass matrix comprising the inertial terms, $\mathbf{C}(\mathbf{q}, \dot{\mathbf{q}})$ is the generalized Coriolis and centrifugal force matrix, $\mathbf{G}(\mathbf{q})$ consisting of all gravitational terms acting on the manipulator, and $(\mathbf{q}, \dot{\mathbf{q}}, \ddot{\mathbf{q}})$ representing the joint variable and its time derivatives. In the case of a 1-DoF manipulator, $\mathbf{q} \in \mathbb{R}$ and it consists of the prismatic joint variable ℓ.
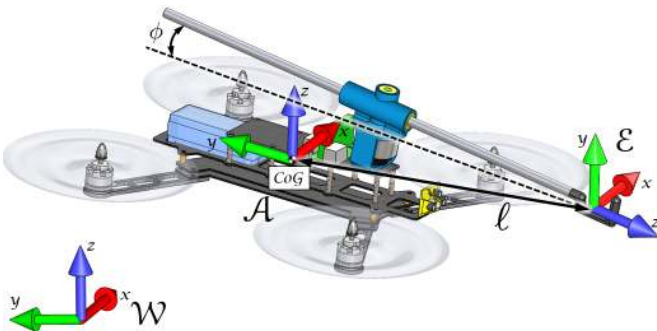
As the manipulator interacts with an obstacle, the forces and moments that generate at the end-effector propagate all the way to the floating base. The combined effect of the aircraft dynamics and the manipulator dynamics, calculated with respect the the body-fixed frame $\mathcal{A}$ yields to:

$$\begin{bmatrix} \mathbf{F}_a(u) \\ \boldsymbol{\tau}_a(u) \end{bmatrix} + \begin{bmatrix} \mathbf{F}_m(\mathbf{q}, \dot{\mathbf{q}}, \ddot{\mathbf{q}}) \\ \boldsymbol{\tau}_m(\mathbf{q}, \dot{\mathbf{q}}, \ddot{\mathbf{q}}) \end{bmatrix} =$$
$$\begin{bmatrix} m\mathbf{R}_{\mathcal{A}}^{\mathcal{W}}\mathbf{e_3} & \mathbf{0} \\ \mathbf{0} & \mathbf{I(q)} \end{bmatrix} \begin{bmatrix} \dot{\mathbf{v}} \\ \dot{\boldsymbol{\omega}} \end{bmatrix} + \begin{bmatrix} 0 \\ \boldsymbol{\omega} \times \mathbf{I(q)}\boldsymbol{\omega} \end{bmatrix} \quad (8)$$

where m represents the UAM overall mass, multiplied by a (3×3) eye matrix $\mathbf{e_3}$ and rotation matrix $\mathbf{R}_{\mathcal{A}}^{\mathcal{W}}$; $\dot{\mathbf{v}}$ and $\dot{\boldsymbol{\omega}}$ are the linear and angular accelerations acting on the UAM, including the linear gravitational term $g = -9.81 \ m/s$, $\mathbf{0}$ is a (3×3) zero matrix and $\mathbf{I(q)}$ is the inertia tensor about frame $\mathcal{A}$. Equation 8 is highly non-linear and describes how the propulsion/actuation system of the aircraft and of the manipulator (left side) counterbalances the linear and angular dynamics (right side).

IV. CONTROL

The envisioned scenario is to be able to install and collect a sensor in the environment, hence the task requires to apply a compression or tension force to a surface. The active slider is used to directly control the interaction force that the UAV is exerting on the wall in a compliant way, as an impedance tool. The force output of the end-effector is the result of the manipulator's active joint and the UAV pitching motion. The interaction with the surface is compliant at first and stiffens slowly as the force builds up. The control architecture, presented in the block diagram of Fig. 5, follows a decentralised approach [1] to take advantage of the high-performance embedded motor controller of the manipulator.

The manipulator inner control loop converts the desired force output into a *current* input for the motor, via a Proportional-Integral (PI) controller. The relation between current and torque generated by the motor is constant and follows the motor's specifications. With the selected motor the torque constant provided by the manufacturer is $K_T = 33.5$ mNm/A. To derive an estimate of the force f_{man} generated by the motor one must consider the efficiency loss in the actuator due to its internal friction ε_e, and the one due to inertia introduced in the system by the gearing in the pinion/rack, ε_m. Both ε_e and ε_m are <1.

$$f_{man} = cK_T\varepsilon_e\varepsilon_m r_p \quad (9)$$

where c is the motor current, r_p is the pinion pitch radius.

Preliminary calibration experiments were run to map the motor *current* into to the resulting force, in static condition. During calibration, the current signal is increased by 100 mA every 5.5 seconds and the force on the sensor is measured, as displayed in Fig. 4 together with the linear interpolation between the variables. It can be observed that the minimum current required to overcome the static friction of the system and sense a force of about 1.6 N is about 200 mA.

The prismatic joint lies on the $z_{\mathcal{E}}$-$y_{\mathcal{E}}$ plane (see Fig. 3), hence the forces generated by the end-effector and propagated to the aircraft will lie on this plane. Now, let us consider a UAV

in contact with a surface by means of a rigid stick, pitching at an angle of θ. The vehicle's own inertia produces a force along the z-axis that is proportional to its weight mg and pitch angle θ:

$$f_{UAV,z} \propto mgtan(\theta) \quad (10)$$

This force contributes towards the total exerted in the environment. To maintain contact with the surface the vehicle must adjust the overall thrust so to counteract the reaction force generated on the obstacle. Hence, Eq. (10) illustrates the static horizontal component of the vehicle's thrust designated to cancel out such reaction force and reach the equilibrium.

The manipulator on-board caters the UAV with an additional DoF and allows for a prompt and quick response as a result of the simpler dynamics governing it. By controlling the interaction force at the end-effector at all times, we are effectively controlling the impedance of the system.

Let us consider the control problem of a floating mass m (UAV) attached to a spring-damper system (manipulator) with stiffness k_m, damping b_m and negligible mass. For the sake of clarity, we consider the UAV as a passive system to which the manipulator is attached. Since the UAV is to be controlled to maintain a desired contact force f_{des} with the environment, the force across the manipulator is $f_{man} = k_m x$, where x is the elongation of the spring. Hence, the physical system is described by:

$$f = m\ddot{x} + k_m x + f_{dist} =$$
$$= mk_m^{-1}\ddot{f}_{man} + f_{man} + f_{dist} =$$
$$= mk_m^{-1}\left[\ddot{f}_{des} + k_{vf}\dot{e}_f + k_{pf}e_f\right] + f_{man} + f_{dist} \quad (11)$$

where f_{dist} is the force due to disturbances, e.g. friction in the manipulator, $e_f = f_{des} - f_{man} - f_{dist}$ is the force error between the desired force f_{des}, the contact force f_{man}, and f_{dist}. Equation 11 is the control law used, with closed-loop system $\ddot{e}_f + k_{vf}\dot{e}_f + k_{pf}e_f = 0$. Now, in static conditions the contact forces do not change over time, except for some oscillations present in the system, therefore we can arbitrarily set $\ddot{f}_{des} = \dot{f}_{des} = \dot{f}_{man} = 0$. Hence rearranging Eq. (11) and including f_{des} in the control law we have:

$$f = mk_{pf}k_m^{-1}e_f + f_{man} + f_{dist}$$
$$= mk_{pf}k_m^{-1}e_f + f_{des} + e_f$$
$$= \left(mk_{pf}k_m^{-1} + 1\right)e_f + f_{des} \quad (12)$$

The UAM control architecture is illustrated in the block diagram of Fig. 5 and follows a decentralised approach [23]
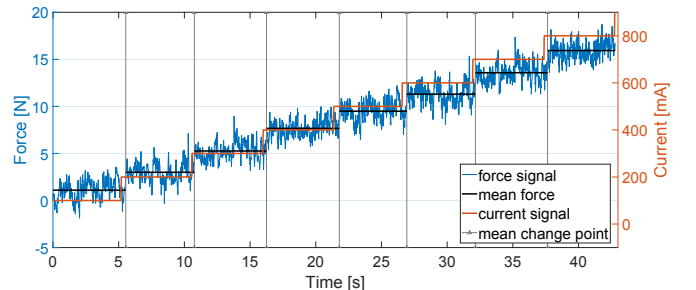

Fig. 4: Calibration of the manipulator in static condition: the motor current (right axis) is compared to the resulting force measured at the Force/Torque sensor (left axis). The relationship between the two variables is linear.

Fig. 5: Block diagram of the control architecture used for the UAM.

Fig. 6: Overview of the aerial manipulator components and setup for flight experiments. The blue boxes highlight the computers/controller boards; the green boxes display the sensing used in the system.

to take advantage of the high performance embedded motor controller of the manipulator. Starting from the left side, the desired force f_{des} is subtracted f_{man}, generating an error e_f that is the input of the proportional control law seen in Eq. (11). The force demand is then converted into a desired *current* value c_{des} and inputted in the motor controller board Maxon EPOS2 24/3 that runs on a Proportional-Integral (PI) control loop at the rate of 10 kHz. The motor board actuates the slider joint and moves the manipulator towards the target, i.e. the environment block. The position, velocity and current states at the end-effector are measured and sent to the *Forward Kinematics* block. The force exerted by the UAV pitching is estimated and corrected with the desired pitch angle $_{des}$. The resulting angle is then converted to force using the mapping seen in the previous section. The task manager and main force controller run on the on-board Raspberry Pi 3. The manipulation task is autonomous and relies on the rangefinder information and the UAV angular states to activate.

V. INDOOR EXPERIMENTS

A total of 48 experiments were conducted indoors to validate installation and retrieval operations on a flat surface. The outline is as follows: the vehicle approaches the contact surface; once the vehicle hovers in a stable way in the proximity of the target, the manipulator triggers autonomously. The manipulation task is activated once specific distance conditions are met on the rangefinder and if the pitch and yaw angles are below a certain threshold. Both these conditions allow to have a repeatable and robust behaviour during flight experiments. The *dummy* sensor used in the experiments is secured on the target surface by means of adhesive pads. For an industrial scenario alternative ways of securing the sensor could be considered, but in conjunction with deployment and retrieval requirements.

A. Experimental Setup

The platform chosen for flight experiments is the quadcopter Lumenier QAV400® (1.1kg), powered by a 4s 2200 mAh battery (250g). The manipulator overall mass is approximately 500g including hardware, electronics and sensing. The aircraft all-up weight is 1.85 kg. The vehicle's autopilot is the Pixhawk 4®. The manipulator is actuated by a direct drive Maxon® motor EC 45 flat (50 Watt, 780 mNm stall torque, 150 g, Hall sensor and encoder) which allows to output high torques and therefore exert considerable force at the end-effector. This motor is controlled by a Maxon® EPOS2 24/3 digital board at a sampling rate of 10 kHz, allowing real-time force

control of the end-effector. A rangefinder TeraRanger® One using Time-of-Flight technology is mounted at the front of the aircraft, sampling at a rate of 1kHz. The manipulator's on-board computer is a Raspberry PI 3 (1.4 GHz 64-bit quad-core ARM Cortex-A53 processor) with Wi-Fi capabilities. The software implementation is in ROS; communication between the Pixhawk and Raspberry PI is through MAVLink/MAVros bridge. A 6-axis Force/Torque sensor Robotiq® FT 300 is mounted on the contact surface and provides ground-truth measurements of the total force exerted by the UAM. Using the convention seen in Fig. 3, F_z is the force normal to the surface and it is the one we wish to control. A VICON® motion capture system acquires ground-truth measurements of the UAV states in-flight. The system architecture and components are displayed in Fig. 6.

B. Sensor Installation Indoors: Results

The objective of these experiments is to validate the bespoke manipulator design and controller for installation tasks that require a considerable exchange of force with the environment. The challenge is to seamlessly combine the force output of the manipulator and of the vehicle in a stable and safe way with a slow force build-up, and to be able to use such force to place a sensor securely onto a flat surface. The second challenge is to control the direction of the force to guarantee a correct installation; if the lateral component of the force is too high due to undesired yaw on the UAV, the end-effector may slip over the target inducing a sudden rotation in the system, leading to failure and potential damage to the UAV. This will be further discussed in the "Outdoor Experiments" section.

Figure 7 illustrates the manipulator's force and displacement (top and middle) and the UAV angular states (bottom), acquired by the Raspberry PI during a single installation task. Figure 8 displays the force along the *x-y-z* axes sensed on the wall by the Force/Torque sensor. Negative values of F_z denote a compression/pushing force on the wall.

To begin with, the end-effector is protruded outwards via a sinusoidal signal in current. The end-effector displaces following the profile seen in Fig. 7, *middle*. The low current that drives the end-effector to the target surface allows for a gentle, compliant touch with the surface and establishes a safe contact. Then, the force is progressively increased to secure the object on the surface and improve the adhesion. Despite the apparent low module on the manipulator's force of approximately 5 N (Fig. 7, *top*), the total force sensed on the

wall reaches -22 N (see Fig. 8) thanks the to aircraft combined pitching motion (see Fig. 7). In this particular experiment, a maximum pitch of 16° is reached. Such inclination, alongside with the manipulator pushing forward, results in a maximum force on the wall of approximately -22 N. It can be noticed that, although the pitch angle goes to zero after approximately 2 seconds, some oscillations in the force are still present on the wall during the *settling* time. This is because the end-effector is still in contact with the wall, transferring part of the UAV motion on the target surface. Such oscillations, however, do not affect the overall outcome or robustness of operation.

In general, the maximum pitch angle measured during the experiments varies between [10°, -20°] and the resulting forces sensed on the wall are between [-12 N, -35 N]. Overall, 33 experiments were carried out to validate indoor installations, with a success rate of 84.8%. Where failure was experienced it was attributed to a positioning error in the *yaw*, which prevented the system from reaching the necessary *pitch* to guarantee adhesion of the sensor on the wall.

C. Sensor Retrieval Indoors: Results

The task begins by flying the UAV close to the target surface, with the end-effector extended outwards. Once the end-effector engages with the sensor placed on the wall, the end-effector retracts and overcomes the wall adhesion. The challenge with retrievals is to guarantee a stable hover in close proximity to the wall, which allows the end-effector to hook

the *dummy* sensor in an accurate way. To facilitate the task and avoid damage of the sensor, the rack is extended and the UAV hovers at maximum available distance from the wall, clear from any turbulence.

From Fig. 9 (*top* figure) it can be observed that the force control on the manipulator perceives an error as it tries to overcome the adhesion force of the object on the wall. The UAV is in position mode and thereby acts in order to minimise the error between the demanded position and the actual position. The resultant UAV pitch angle during the operation (Fig. 9, *bottom*) therefore becomes negative as it rotates anticlockwise in an attempt to pull the sensor away. Once again the resultant UAV motion, combined with the manipulator action results in a tension force applied to the wall of up to 8 N, see Fig. 10. The resultant force has positive sign as to indicate tension on the Force/Torque sensor. As the object is collected, pitch oscillations can be seen, as during the installation phase. These are a consequence of the UAV settling down and counteracting the sudden change in inertia after the sensor detaches from the wall. Overall, the oscillations sensed are below 5°; and the success rate over 15 experiments was found to be 100%.

VI. OUTDOOR EXPERIMENTS

A total of 41 outdoor experiments were performed to test the system in more complex conditions. The selected target

Fig. 7: Sensor installation indoors - data collected by the on-board Raspberry PI. From top to bottom: pushing force exerted by the manipulator, end-effector displacement and UAV angular states.
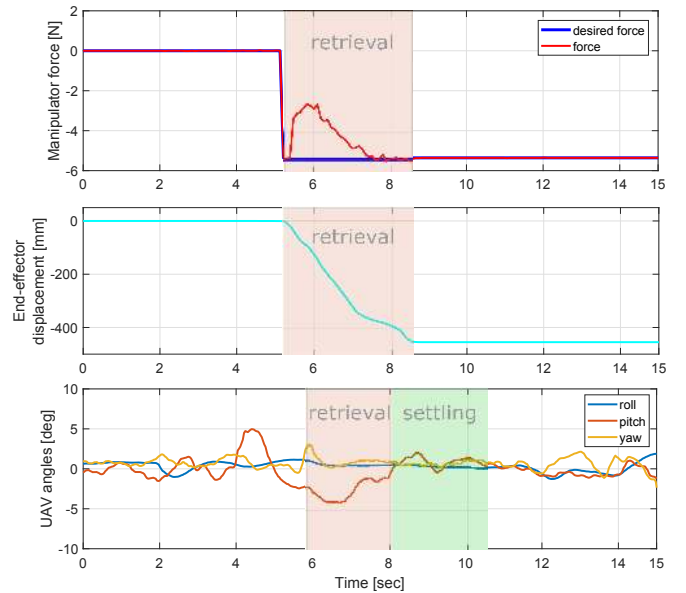

Fig. 9: Sensor retrieval indoors - data collected by the on-board Raspberry PI. From top to bottom: pulling force exerted by the manipulator, end-effector displacement and UAV angular states.

Fig. 8: Force measurements from the Force/Torque sensor during a single installation.
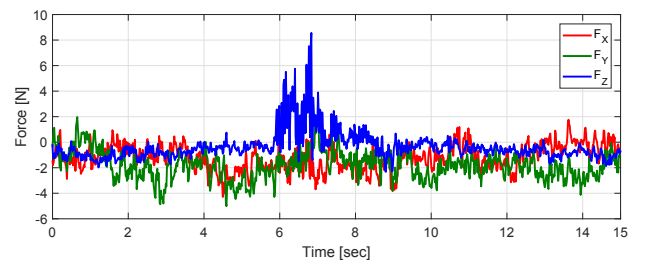

Fig. 10: Force measurements from the Force/Torque sensor during a retrieval task.

for outdoor operations was a cylindrical, irregular surface, i.e. a tree trunk. The envisioned application is the installation and retrieval of sensors on trees to prevent forest fires and to achieve real-time monitoring and surveying. In addition, this scenario is more complex than other potential applications - thereby providing a realistic but challenging test scenario.

The experimental setup used is similar to the one seen previously, except for the lack of the VICON tracker reading the UAV states, and the Force/Torque sensor measuring the contact force. GPS signal was instead used to conduct outdoor experiments, and the vehicle was piloted towards the target in position mode. Flying outdoors brings additional challenges such as accurate pose estimation of the aircraft and the induced disturbances/turbulence by unknown obstacles. The purpose of these tests was therefore to demonstrate if placement and recovery is in essence feasible and to identify the best approach to take in order to improve reliability.

A. Sensor Installation Outdoors: Results

For outdoor experiments, the *current* input used to extend and retract the end-effector was generally lower when compared to the indoor flights. This was chosen so as to increase the compliance of the end-effector when in contact with the tree and to have a less aggressive behaviour. Once contact is established, the UAV progressively increases its pitch to generate a good adhesion on the object, then flies backwards after a successful placement.

Results are illustrated in Fig. 11. The *top* figure shows the manipulator force during the task: contact with the tree occurs at t = 4 s, where the impact of the object on the target surface generates a force error in the controller. During this time, the manipulator is still extending (see *middle* figure) and the UAV's CoG moves backwards. This phenomenon occurs anytime the UAV horizontal thrust component is lower than the manipulator's force, causing the aircraft to respond. A clear visual demonstration of this is captured in the video

attachment. In general, the pitch angle reached during outdoor experiments ranges between [10°,-15°].

Another behaviour typical of outdoor experiments is the longer settling time needed by the UAV to recover to the hover. As previously discussed, one of the major factors that plays a role in pose estimation is the use of GPS over the VICON motion tracker. One potential source for the increased settling times noted outdoors is the presence of gusts and other obstacles that induce turbulence, e.g. surrounding trees, branches. In general, this had minimal effect on the overall success rate - with the main cause for failure being an undesired yaw during contact, which induced lateral forces in the end-effector and slippage. 23 experiments were performed and a success rate of 78.2% was measured.

B. Sensor Retrieval Outdoors: Results

Outdoor retrieval experiments were carried in the same way as indoors. Results are shown in Fig. 12. In general, the same challenges as the indoor setting were present, however the GPS-based flight made long-term stable hovering in the proximity of the sensor more challenging outdoors as opposed to indoors. Also, the settling time during recovery is longer, as with outdoor installations. Often, the pitch angle oscillates between [-10°,10°] after retrieving the object from the wall, with oscillations also present in yaw. Despite these oscillations, the overall success rate in outdoor retrievals is 100% over 18 experiments performed.

Outdoor experiments demonstrated the feasibility and robustness of the proposed approach for both placement and retrieval tasks. The conclusions drawn from these experiments showed that a stable hover and a more compliant behaviour were key elements to succeed in the outdoor setting. In particular, the demanded force output of the aerial system was lowered, as it was the one of the manipulator. Lower *pitch* was reached to compensate for the less accurate GPS-based
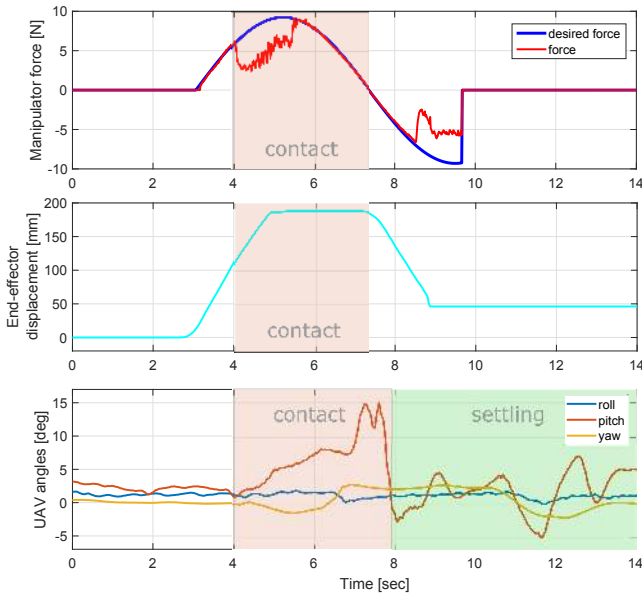

Fig. 11: Sensor installation outdoors - data collected by the on-board Raspberry PI. From top to bottom: pushing force exerted by the manipulator, end-effector displacement and UAV angular states.
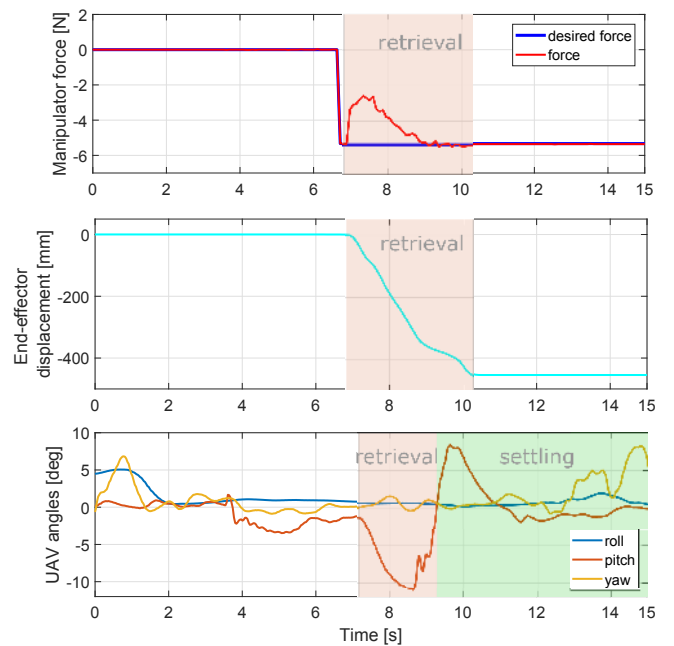

Fig. 12: Sensor retrieval outdoors - data collected by the on-board Raspberry PI. From top to bottom: pulling force exerted by the manipulator, end-effector displacement and UAV angular states.

pose estimation, and this allowed to have a less aggressive behaviour on the aircraft. Overall, the installation task proved more complex than the retrieval, in both indoor and outdoor settings, because of the dynamic nature of the task itself. Nonetheless, good results were achieved and considerable forces were exerted by the small-sized UAM.

VII. CONCLUSIONS

This paper presents a novel approach to aerial installation and retrieval operations with the use of a single-DoF compliant manipulator. Despite the limited dexterity of the proposed manipulator design, we are able to demonstrate its versatility for force-driven operations such as the placement of objects on surfaces of different shape and texture. The design strength lies in the simplicity of the transmission mechanism and its minimal weight, which make it suitable for on-site inspection, NDT operations, or simply as a modular tool that provides the aerial platform with active tactile feedback. The actuation of the slider joint guarantees the ability to adjust the compliant behaviour of the end-effector in real-time, providing higher compliance at the touch and a stiffer response for more accurate positioning. Real-time force control was found to be an essential feature for the manipulator to safely interact in-flight, leading to a higher robustness measured during flight tests. The novelty of our approach lies in the integration of the force-controlled manipulator with the UAV pitching motion for slow force build-up outputs. Both the design and the control architecture are successfully tested indoors for operations over flat vertical surfaces, and outdoors over irregular surfaces. Numerous experiments validate the reliability and repeatability of the system. Overall the proposed approach demonstrates a great potential for low-dexterity manipulation tasks, such as the application of forces in the environment for probing, NDT, object installation and retrieval.

Further work will address the refinement of the flight controller with the use of Model Predictive Control methods (MPC) in order to minimise the vehicle's angular disturbances during interaction. Moreover, the design of new grippers will be evaluated to stretch the number of applications that can be achieved with the proposed manipulator, together with additional sensory feedback solutions that could improve the performance and refine the autonomous behaviour, e.g. event-based cameras.

ACKNOWLEDGMENT

REFERENCES

[1] F. Ruggiero, V. Lippiello, and A. Ollero, "Aerial manipulation: A literature review," *IEEE Robotics and Automation Letters*, vol. 3, no. 3, pp. 1957–1964, 2018.

[2] P. E. Pounds, D. R. Bersak, and A. M. Dollar, "Grasping from the air: Hovering capture and load stability," in *Robotics and Automation (ICRA), 2011 IEEE International Conference on*, pp. 2491–2498, IEEE, 2011.

[3] F. Augugliaro, S. Lupashin, M. Hamer, C. Male, M. Hehn, M. W. Mueller, J. S. Willmann, F. Gramazio, M. Kohler, and R. D'Andrea, "The flight assembled architecture installation: Cooperative construction with flying machines," *Control Systems, IEEE*, vol. 34, pp. 46–64, 2014.

[4] G. Loianno, V. Spurny, J. Thomas, T. Baca, D. Thakur, D. Hert, R. Penicka, T. Krajnik, A. Zhou, A. Cho, *et al.*, "Localization, grasping, and transportation of magnetic objects by a team of mavs in challenging desert like environments," *IEEE Robotics and Automation Letters*, vol. 3, no. 3, pp. 1576–1583, 2018.

[5] "AIRobots," 2012. http://airobots.ing.unibo.it/.

[6] "AEROWORKS," 2015. http://www.aeroworks2020.eu/.

[7] "AEROARMS," 2015. https://aeroarms-project.eu/.

[8] I. Palunko, P. Cruz, and R. Fierro, "Agile load transportation: Safe and efficient load manipulation with aerial robots," *IEEE Robotics & Automation Magazine*, vol. 19, no. 3, pp. 69–79, 2012.

[9] M. Fumagalli, R. Naldi, A. Macchelli, F. Forte, A. Q. Keemink, S. Stramigioli, R. Carloni, and L. Marconi, "Developing an aerial manipulator prototype: Physical interaction with the environment," *Robotics & Automation Magazine, IEEE*, vol. 21, pp. 41–50, 2014.

[10] M. Orsag, C. Korpela, S. Bogdan, and P. Oh, "Valve turning using a dual-arm aerial manipulator," in *Unmanned Aircraft Systems (ICUAS), 2014 International Conference on*, pp. 836–841, IEEE, 2014.

[11] T. Ikeda, S. Yasui, M. Fujihara, K. Ohara, S. Ashizawa, A. Ichikawa, A. Okino, T. Oomichi, and T. Fukuda, "Wall contact by octo-rotor uav with one dof manipulator for bridge inspection," in *Intelligent Robots and Systems (IROS), 2017 IEEE/RSJ International Conference on*, pp. 5122–5127, IEEE, 2017.

[12] F. Huber, K. Kondak, K. Krieger, D. Sommer, M. Schwarzbach, M. Laiacker, I. Kossyk, S. Parusel, S. Haddadin, and A. Albu-Schaffer, "First analysis and experiments in aerial manipulation using fully actuated redundant robot arm," in *Intelligent Robots and Systems (IROS), 2013 IEEE/RSJ International Conference on*, pp. 3452–3457, IEEE, 2013.

[13] S. Kim, S. Choi, and H. J. Kim, "Aerial manipulation using a quadrotor with a two dof robotic arm," in *Intelligent Robots and Systems (IROS), 2013 IEEE/RSJ International Conference on*, pp. 4990–4995, IEEE, 2013.

[14] C. Huerzeler, R. Naldi, V. Lippiello, R. Carloni, J. Nikolic, K. Alexis, L. Marconi, and R. Siegwart, "Airobots: Innovative aerial service robots for remote inspection by contact," in *Intelligent Robots and Systems (IROS), 2013 IEEE/RSJ International Conference on*, pp. 2080–2080, IEEE, 2013.

[15] A. Suarez, G. Heredia, and A. Ollero, "Lightweight compliant arm for aerial manipulation," in *Intelligent Robots and Systems (IROS), 2015 IEEE/RSJ International Conference on*, pp. 1627–1632, IEEE, 2015.

[16] J. L. Scholten, M. Fumagalli, S. Stramigioli, and R. Carloni, "Interaction control of an uav endowed with a manipulator," in *Robotics and Automation (ICRA), 2013 IEEE International Conference on*, pp. 4910–4915, IEEE, 2013.

[17] M. Ryll, G. Muscio, F. Pierri, E. Cataldi, G. Antonelli, F. Caccavale, and A. Franchi, "6d physical interaction with a fully actuated aerial robot," in *2017 IEEE International Conference on Robotics and Automation*, 2017.

[18] T. Bartelds, A. Capra, S. Hamaza, S. Stramigioli, and M. Fumagalli, "Compliant aerial manipulators: Toward a new generation of aerial robotic workers," *IEEE Robotics and Automation Letters*, pp. 477–483, Jan 2016.

[19] S. Hamaza, I. Georgilas, and T. Richardson, "Towards an adaptive-compliance aerial manipulator for contact-based interaction," in *2018 IEEE/RSJ International Conference on Intelligent Robots and Systems (IROS)*, pp. 1–9, IEEE, 2018.

[20] C. Papachristos, K. Alexis, and A. Tzes, "Efficient force exertion for aerial robotic manipulation: Exploiting the thrust-vectoring authority of a tri-tiltrotor uav," in *Robotics and Automation (ICRA), 2014 IEEE International Conference on*, pp. 4500–4505, IEEE, 2014.

[21] H. W. Wopereis, J. Hoekstra, T. Post, G. A. Folkertsma, S. Stramigioli, and M. Fumagalli, "Application of substantial and sustained force to vertical surfaces using a quadrotor," in *2017 IEEE International Conference on Robotics and Automation (ICRA)*, pp. 2704–2709, IEEE, 2017.

[22] S. Hamaza, I. Georgilas, and T. Richardson, "An adaptive-compliance manipulator for contact-based aerial applications," in *2018 IEEE/ASME International Conference on Advanced Intelligent Mechatronics (AIM)*, pp. 730–735, IEEE, 2018.

[23] A. Jimenez-Cano, J. Martin, G. Heredia, A. Ollero, and R. Cano, "Control of an aerial robot with multi-link arm for assembly tasks," in *Robotics and Automation (ICRA), 2013 IEEE International Conference on*, pp. 4916–4921, IEEE, 2013.